Gelatin-Oxidized Nanocellulose Hydrogels Suitable for Extrusion-Based 3D Bioprinting

Authors:

Shiyu Zhou, Chenyang Han, Zhongjin Ni, Chao Yang, Yihua Ni, Yan Lv

Date Submitted: 2023-02-20

Keywords: 3D bioprinting, oxidized nanocellulose, gelatin, glycerol, hydrogel, printability

Abstract:

3D bioprinting is an emerging research field developed by the deep cross-fertilization of 3D printing technology with multiple disciplines such as mechanics, materials, and biomedicine. Extrusion 3D bioprinting, the most widely used 3D bioprinting technology, can print biomaterials with different viscosities and has a wide range of material applicability. In this study, we prepared a composite hydrogel with gelatin-oxidized nanocellulose as the matrix and glycerol as a multifunctional co-solvent, and the optimal composition of the hydrogel was determined by material characterization. The microstructure of the hydrogel was visualized by scanning electron microscopy (SEM), and it can be seen that the composite hydrogel material has a three-dimensional porous network structure with microporous pore sizes ranging from 200?300 μm. The infrared spectra also showed that the addition of glycerol did not interact with gelatin-oxidized nanocellulose while improving the hydrogel properties. Meanwhile, the composite hydrogel has obvious shear-thinning properties and good mechanical properties, which are suitable for extrusion-based 3D bioprinting, and the printed area is clear and structurally stable. A series of results indicate that the hydrogel is suitable for extrusion-based 3D bioprinting with good pore structure, mechanical properties, and printable performance. This gelatin-oxidized nanocellulose hydrogel provides a new idea and material for 3D bioprinting and expands the potential uses of the material.

Record Type: Published Article

Submitted To: LAPSE (Living Archive for Process Systems Engineering)

Citation (overall record, always the latest version):	LAPSE:2023.0735
Citation (this specific file, latest version):	LAPSE:2023.0735-1
Citation (this specific file, this version):	LAPSE:2023.0735-1v1

DOI of Published Version: https://doi.org/10.3390/pr10112216

processes

MDPI

Article

Gelatin-Oxidized Nanocellulose Hydrogels Suitable for Extrusion-Based 3D Bioprinting

Shiyu Zhou, Chenyang Han, Zhongjin Ni *, Chao Yang, Yihua Ni and Yan Lv

College of Optical, Mechanical, and Electrical Engineering, Zhejiang Agriculture and Forestry University, Hangzhou 311300, China

* Correspondence: 20010049@zafu.edu.cn

Abstract: 3D bioprinting is an emerging research field developed by the deep cross-fertilization of 3D printing technology with multiple disciplines such as mechanics, materials, and biomedicine. Extrusion 3D bioprinting, the most widely used 3D bioprinting technology, can print biomaterials with different viscosities and has a wide range of material applicability. In this study, we prepared a composite hydrogel with gelatin-oxidized nanocellulose as the matrix and glycerol as a multifunctional co-solvent, and the optimal composition of the hydrogel was determined by material characterization. The microstructure of the hydrogel was visualized by scanning electron microscopy (SEM), and it can be seen that the composite hydrogel material has a three-dimensional porous network structure with microporous pore sizes ranging from 200–300 μm. The infrared spectra also showed that the addition of glycerol did not interact with gelatin-oxidized nanocellulose while improving the hydrogel properties. Meanwhile, the composite hydrogel has obvious shear-thinning properties and good mechanical properties, which are suitable for extrusion-based 3D bioprinting, and the printed area is clear and structurally stable. A series of results indicate that the hydrogel is suitable for extrusion-based 3D bioprinting with good pore structure, mechanical properties, and printable performance. This gelatin-oxidized nanocellulose hydrogel provides a new idea and material for 3D bioprinting and expands the potential uses of the material.

Keywords: 3D bioprinting; oxidized nanocellulose; gelatin; glycerol; hydrogel; printability

Citation: Zhou, S.; Han, C.; Ni, Z.; Yang, C.; Ni, Y.; Lv, Y. Gelatin-Oxidized Nanocellulose Hydrogels Suitable for Extrusion-Based 3D Bioprinting. *Processes* **2022**, *10*, 2216. https://doi.org/10.3390/pr10112216

Academic Editor: Sara Liparoti

Received: 1 October 2022
Accepted: 25 October 2022
Published: 27 October 2022

1. Introduction

3D printing, as one type of Additive Manufacturing (AM), is characterized by the construction of three-dimensional solids by stacking layers and allows the fabrication of custom or complex structures without the need for expensive and time-consuming mold-making procedures [1] and is widely used in aerospace, architecture, process design, education, medical, and biological fields [2–4]. Biological 3D printing is an emerging research field developed by combining 3D printing technology with biomedicine [5], which can manufacture scaffolds with high structural complexity and design flexibility, thus overcoming the limitations of traditional tissue engineering, and is a perfect combination of biomedicine, tissue engineering, regenerative medicine, and 3D printing technology, which can achieve spatially oriented manipulation of biological materials, growth factors, cells, and controlled stacking, solving the challenges faced by traditional tissue engineering [6], which has important research significance and broad application prospects [7,8].

Depending on the forming principle and printing materials, 3D bioprinting technologies can be subdivided into four types: inkjet, laser direct writing, light-curing, and extrusion printing [9–12]. The principle of the four printing types is shown in Figure 1.

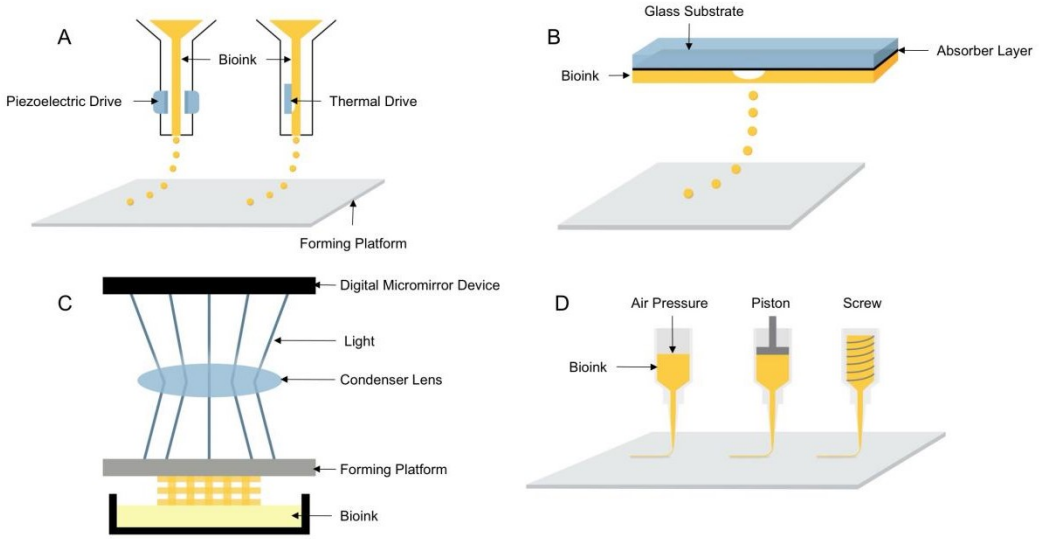

Figure 1. Schematic diagram of the four 3D bioprinting technologies: (**A**) inkjet 3D bioprinting, (**B**) laser direct writing 3D bioprinting, (**C**) light-curing 3D bioprinting, (**D**) extrusion 3D bioprinting.

Inkjet 3D bioprinting is considered to be the earliest 3D bioprinting technology that uses piezoelectric or thermally driven printheads to dispense bioinks into a series of micro-droplets that are printed in layers to shape the 3D structures containing cells [13]. Inkjet printing has the advantages of being able to install multiple printheads and faster printing speed and is the least costly 3D bioprinting technique. However, it has disadvantages, such as the inability to print highly viscous materials and highly concentrated bioinks and mechanical or thermal damage to cells during the printing process. Compared with inkjet printing, laser direct printing can avoid direct contact between the bioink and the processing device, thus ensuring high cell activity, and can also print high viscosity bioinks and use a wider range of materials, but it has the disadvantage of higher printing cost. Similar to laser direct printing, light-cured printing uses light to selectively cross-link bioinks, curing them in layers to form three-dimensional structures. Light-cured printing has the advantages of high printing efficiency and accuracy [14] and is a simple device for easy control, but UV light and photoinitiators can cause damage to cells. Extrusion printing is the most widely used 3D bioprinting technology [15], which evolved from inkjet printing and extruded uninterrupted fibrous filaments by continuous extrusion force [16] and has the advantages of printing bioink with different viscosities and different concentrations of cells, a wide range of material applicability, and the ability to print tissue structures with good structural strength. Since inkjet, laser direct writing, and light-curing 3D bioprinting technologies have high requirements for printing materials, printing processes, and molding equipment, and the application range is relatively narrow, most of the printing equipment based on these technologies are built independently and are still in the laboratory research stage, and no mature printing equipment has been reported. Therefore, the extrusion 3D bioprinting method was used in this study to investigate the performance of hydrogel printing.

Bioinks suitable for extrusion-based 3D bioprinting need to meet three conditions. First, shear-thinning properties. This is a rapid sol-gel transition capability (smooth extrusion from the nozzle can be rapidly shaped on the deposition platform) [17]. Second, good mechanical properties. This ensures the stability of the printed structure [18]. Third, excellent biocompatibility [19]. As a unique class of 3D polymer network "soft" materials, hydrogels have excellent toughness, elasticity, and flexibility, as well as good mechanical strength, optical transparency, biodegradability, and biocompatibility, making them suitable for extruded 3D bioprinting of bioinks, which are widely used in agriculture, industry, and biomedical fields [20–22].

The most used hydrogel compositions in studies on extrusion 3D bioprinting available hydrogels are sodium alginate (SA) and gelatin (GEL) because these two natural materials

have good shear-thinning properties [23] and biocompatibility. GEL is a protein obtained by partial hydrolysis of collagen, which has excellent biocompatibility and cell adhesion properties. By co-blending GEL with SA, the temperature-controlled cross-linking property of GEL and the cross-linking property of SA with divalent cations can be well applied to extrusion-based biological 3D printing. However, this hydrogel has the problems of high viscosity leading to damage to cells due to excessive air pressure during the printing process and low dry matter content leading to print collapse, thus seriously affecting the shape fidelity.

SA has some thickening properties and has a high viscosity at low concentrations. Thus, in this study, we used only one material, GEL, to provide shear-thinning properties, thereby reducing the hydrogel viscosity and decreasing the air pressure required for printing. Studies have shown that the addition of small amounts of nanoparticles to hydrogels can lead to significant changes in a range of physical and chemical properties, such as an increase in material stiffness and the appearance of shear-thinning properties. In recent years, nanocellulose-based hydrogels have attracted a lot of attention in the field of tissue engineering due to their unique nanostructures, excellent mechanical properties, and good biocompatibility [24,25]. Some recent articles have also proposed some hydrogel formulations based on the incorporation of nanocellulose in alginate for biomedical applications, but only the formulation composition was described without an in-depth study. In this study, we used TEMPO system oxidized nanocellulose (T-CNF), which can effectively avoid agglomeration of nanocellulose and improve its dispersion and stability in water and enhance the stability and mechanical properties of gelatin-based hydrogels.

Collapse is a typical characteristic of bio-based hydrogels, usually due to low dry matter content. In order to avoid structural collapse after printing, in this study, we replaced part of the water with glycerol (GLY) to reduce the volume and share of non-volatile components to minimize excessive shrinkage and to allow the samples to retain their shape after curing. It was demonstrated that the addition of food-grade additives such as glycerol, sugar, and citric acid to gelatin does not compromise the biocompatibility and safety of the material while producing gel compositions with elasticity and toughness [26,27]. The addition of GLY to the hydrogel also enhances the stability and water retention of the hydrogel since the gelatin-based hydrogel can harden in the air due to rapid drying, which affects its stability and durability as a bioprinting material.

In this study, a biocompatible composite hydrogel based on GEL, T-CNF, and GLY was prepared for 3D bioprinting. The addition of T-CNF and GLY can not only adjust the viscosity of the hydrogel but also enhance the mechanical properties. Through morphological observation, chemical structure characterization, rheological property test, mechanical property test, and swelling performance test, the influence of GLY on various properties of the hydrogel was analyzed, and the optimal proportion of each component of the hydrogel was determined. Finally, the hydrogel was applied to extrusion bioprinting, showing excellent printability and shape fidelity while also being more stable at room temperature.

2. Materials and Methods

2.1. Materials

Gelatin (GEL), Sinopharm Chemical Reagent Co., Ltd., Shanghai, China; Glycerin (GLY), Shanghai McLean Biochemical Technology Co., Ltd., Shanghai, China; TEMPO system oxidized nanocellulose (T-CNF), Tianjin Wood Spirit Biotechnology Co., Ltd., Tianjin, China; Glutaraldehyde (GA), Shanghai Aladdin Biochemical Technology Co., Ltd, Shanghai, China. The deionized water was used in all experiments. All reagents were used directly without any further treatment.

2.2. Preparation of Hydrogels

Gelatin and oxidized nanocellulose were used as composite hydrogel matrices, and the content of the multifunctional co-solvent glycerol was varied to prepare different kinds of hydrogels. The initial experimental goal was to configure hydrogels with the right viscosity

so that the hydrogels could be extruded smoothly through the print nozzle and retain their shape and structure on the deposition platform. After the preliminary experiments, four hydrogels with different composition ratios were selected for the next evaluation (Table 1).

Table 1. Hydrogel formulation.

Sample ID	Gelatin (% *w*/*v*)	T-CNF (% *w*/*v*)	Glycerin (% *w*/*v*)	Deionized Water (% *w*/*v*)
GTG0	8	1	0	91
GTG10	8	1	10	81
GTG30	8	1	30	61
GTG50	8	1	50	41

The T-CNF powder was first dissolved in deionized water, sonicated for 30 min, and then magnetically stirred for 2 h to obtain a uniformly dispersed, transparent gelatinous suspension of T-CNF. Gelatin and glycerol were then added to the oxidized nanocellulose suspension and magnetically stirred for 12 h. The covered glass beaker was kept at 37 °C throughout the magnetic stirring process. All hydrogels were stored in a water bath at 37 °C before further testing or printing.

2.3. Morphological and Chemical Characterization of Hydrogels

2.3.1. Macroscopic Topography of Hydrogels

The composite hydrogels configured after ultrasonic dispersion and magnetic stirring were left to stand for one hour at 37 °C in a water bath to observe the dispersion of the materials. Then the hydrogel was poured into a cylindrical mold with an inner diameter of 15 mm and a height of 10 mm, put into a refrigerator at 4 °C for 1 h, and then removed from the mold to observe the macroscopic morphology of the hydrogel after low-temperature curing.

2.3.2. Scanning Electron Microscope Testing of Hydrogels

The cryogenically cured cylindrical hydrogel samples were cross-linked by immersion in 2% *w*/*v* glutaraldehyde (GA) solution for 24 h, then pre-frozen overnight at −20 °C and placed in a freeze dryer (ALPHA 2–4 LD plus, Marin Christ, Ltd., Osterode, Germany) with a cold trap temperature of −70 °C. The lyophilized hydrogels were cut horizontally, sprayed with gold, and observed using an ultra-high resolution field emission scanning electron microscope (SU8020, Hitachi, Ltd., Tokyo, Japan) with an accelerating voltage of 5 kV.

2.3.3. Chemical Structural Characterization of Hydrogels

The functional group changes of the hydrogels were tested using Fourier transform infrared (FT-IR) spectrometer (Nicolet iS10, Thermo Fisher Scientific, Ltd., Waltham, MA, USA), and the test samples were prepared by KBr (Sinopharm Chemical Reagent, Ltd., Shanghai, China) compression method. The scanning range was set to 500–4000 $cm^{-1,}$ and the resolution was set to 4 cm^{-1}.

2.4. Rheological Properties Testing of Hydrogels

A certain amount of uncross-linked hydrogel was tested for rheological properties (MCR 92, Anton Paar, Ltd., Graz, Austria). The shear rate-viscosity curves were scanned at a steady rate in the shear rate range of 1 s^{-1} to 500 s^{-1}. A 40 mm diameter parallel plate (with a 2 mm gap) was used to simulate the viscosity of the material at the syringe and nozzle during the printing process, and the temperature was kept at 37 °C during the test. The velocity of the plate adopted to reach the selected gap was varied from 0.15 to 0.60 mm/s, and the normal force was recorded with the aim of eliminating the effect of the compression on the structure and rheology of the hydrogel. Before starting rheological tests, the sample was left to relax with normal force, and then the excess material was removed. The oscillation-frequency scanning angular frequency range was 0.1–100 rad/s

with 1% strain, and the temperature was maintained at 37 °C during the test. Oscillation-temperature scan angular frequency of 1 rad/s, strain 1%, temperature range of 10–50 °C.

2.5. Mechanical Properties Testing of Hydrogels

The prepared hydrogels were cast on cylindrical molds with an inner diameter of 15 mm and a height of 10 mm, refrigerated at 4 °C for 1 h until the gel structure was stable, and then cross-linked in 2% w/v glutaraldehyde (GA) solution for 24 h. After the cross-linking was completed, the samples were removed, and the surface water was blotted with filter paper to obtain a uniform and stable cylindrical sample. The compression performance was tested using ASTM F2150-19 standard, using a universal testing machine (CMT6104, MTS Industrial Systems Co., Ltd., Shenzhen, China) with the sample placed in the center of two cylindrical compression plates with a compression displacement rate of 0.5 mm/min until the sample ruptured. Each set of tests was repeated five times.

2.6. Swelling Performance Test of Hydrogels

The hydrogel samples were freeze-dried in a freeze-dryer at a cold trap temperature of −70 °C for 24 h and then removed, and the weight of the freeze-dried gel was weighed as W_0. The gel was then swollen in deionized water at room temperature and removed at regular intervals (1, 3, 5, 7, 12, and 24 h) and the surface water was wiped dry with filter paper and weighed, and the real-time mass was recorded as W_t to calculate the Swelling Ratio (SR) of the gel.

$$SR(\%) = \frac{W_t - W_0}{W_0} \times 100\% \quad (1)$$

After 24 h, the gel was weighed continuously until the gel weight stopped changing, which was recorded as the gel swelling equilibrium weight Ws, and the swelling ratio at this time was recorded as Equilibrium Swelling Ratio (ESR).

2.7. Printing Performance Test of Hydrogels

A desktop bioprinter (EFL-BP-6800, Suzhou Intelligent Manufacturing Research Institute, Suzhou, China) was used to perform the printing performance test of hydrogels. The bioprinter consists of a screw-driven X-Y-Z moving system, a pneumatic micro-extrusion system (0–30 kPa), a temperature control system (−10–70 °C), and a control management system. The temperature control system at the nozzle ensures that the hydrogel is extruded smoothly at a suitable temperature, and the cooling system of the printing platform ensures the stability of the structure after the hydrogel is extruded and formed. Before the bioprinting starts, the drawn model is imported into specific software, and after adjusting the parameters, the 3D structure is printed by using the Slic3r slicing engine to slice the 3D model and generate the code or by editing the G code by itself.

This part of the test mainly investigates the differences in the printing performance of different formulations of hydrogels. Thus, the other parameters of the printing process were kept unchanged, and only the printing material was changed. The extrusion head temperature was 37 °C; the printing platform temperature was 5 °C; the nozzle travel speed was 5 mm/s; the nozzle diameter was 0.26 mm; the height of the nozzle from the printing platform was 0.3 mm, and other parameters such as the filling method were also kept unchanged.

3. Results and Discussion

3.1. Analysis of Morphological and Chemical Characterization Results of Hydrogels

3.1.1. Morphology Analysis of Hydrogels

As shown in Figure 2, the hydrogels were uniform and stable after ultrasonic dispersion and magnetic stirring, and no precipitation was found after a long period of resting, indicating that the components within the hydrogels were evenly dispersed and stable in nature. The cast hydrogel has a smooth surface and smooth demolding after being refrigerated for 1 h, showing good toughness and stability. Since the GEL is a pale yellow

particle, the hydrogel also exhibits a corresponding degree of pale yellow. With the increase in GLY content, it can be found that the air bubbles inside the hydrogel gradually increased, which may be due to the increase in the overall viscosity of the hydrogel resulting in the slow discharge of the air mixed in the long mixing process. To avoid the effect of air bubbles on other performance tests of the hydrogel, we will subsequently perform the extraction process to eliminate the air bubbles in the hydrogel.

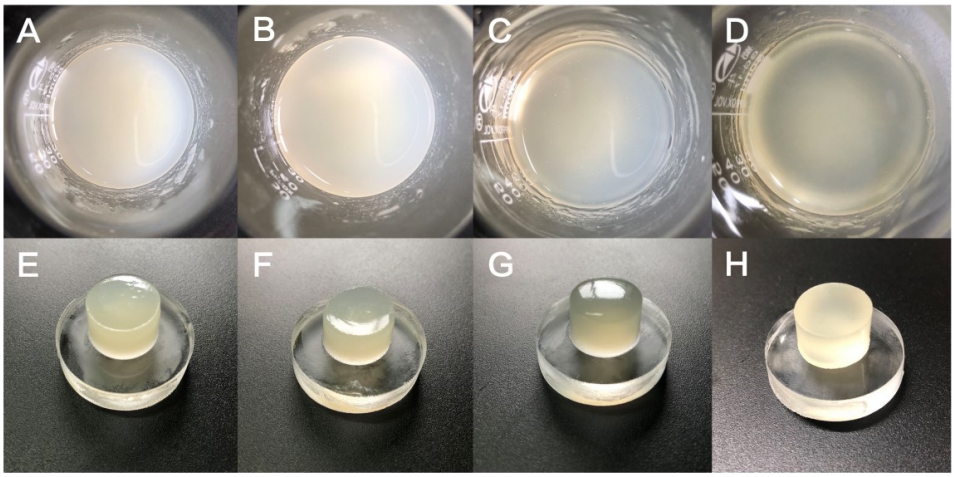

Figure 2. (**A**) GTG0 solution, (**B**) GTG10 solution, (**C**) GTG30 solution, (**D**) GTG50 solution, (**E**) GTG0 after low-temperature cross-linking, (**F**) GTG10 after low-temperature cross-linking, (**G**) GTG30 after low-temperature cross-linking, (**H**) GTG50 after low-temperature cross-linking.

It can also be found that when the GLY content is 0, the hydrogel behaves milky white and yellowish; when GLY is dissolved in hydrogel, and the content is increasing, the hydrogel gradually becomes clear and transparent. This may be due to the stabilization of the interaction between glycerol, water, and the polymer network. Macroscopic morphological analysis shows that the addition of GLY has a stabilizing effect on the hydrogel and does not affect the gel properties.

3.1.2. Analysis of the Results of Scanning Electron Microscopy of Hydrogels

The significant differences in properties exhibited by composite hydrogels are mainly related to their microstructural variations. Therefore, the microstructure of hydrogels can be visualized by the scanning electron microscopy (SEM) technique, which can reflect the internal cross-linking of hydrogels and observe the microporous structure morphology and composition of solid substances.

Figure 3 shows the SEM images of the hydrogel samples after freeze-drying. It can be seen that the composite hydrogel materials prepared in this study have a three-dimensional porous network structure with micropores sizes ranging from 200–300 μm. The pore sizes of GTG0 are different and not uniformly dispersed; with the addition of GLY and the increase in concentration, the micropores of the composite hydrogel are gradually evenly distributed and uniform in pore size. GTG30 has uniform distribution and a moderate number of micropores with good structure and porosity, which can make the balance between mechanical properties and material transport of the composite hydrogel. GTG50 has too dense micropores, which will negatively affect the mechanical properties of the hydrogel.

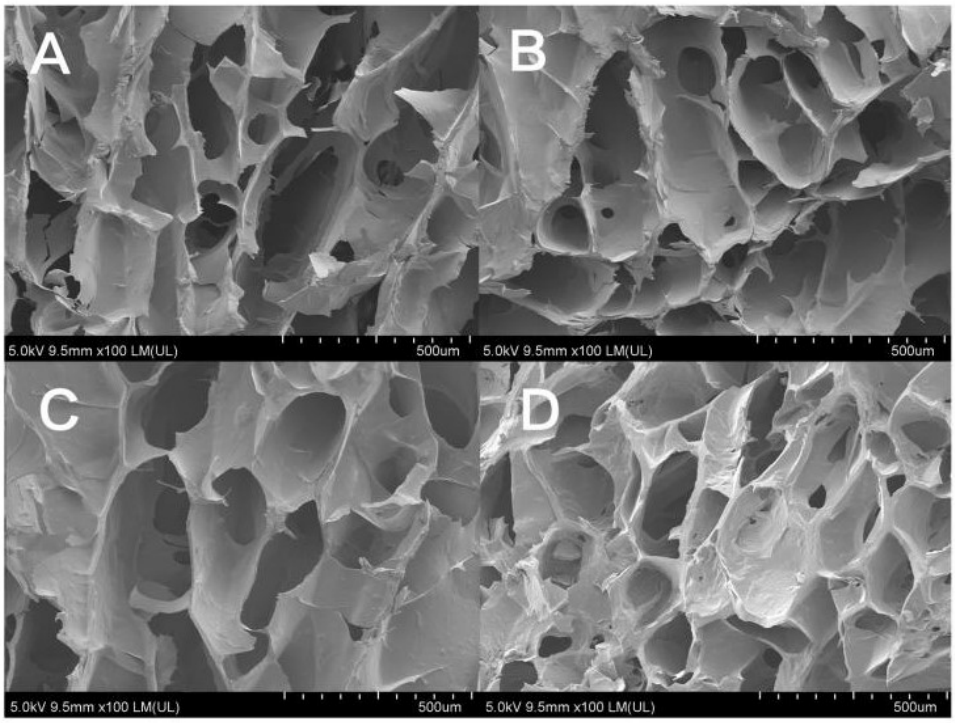

Figure 3. SEM images of hydrogels: (**A**) GTG0, (**B**) GTG10, (**C**) GTG30, and (**D**) GTG50.

The microporous structure of GTG30 is partly open-cells and partly closed-cells. The presence of both types of micropores can provide growth space and material transport channels for cell proliferation and adhesion, and the geometry, porosity, and pore size of micropores can directly affect cell behavior. High porosity and pore size help nutrient and oxygen transport or enable more cells to grow inward, but the mechanical properties of the hydrogel can be compromised if the pore volume is too large. All these qualities lay the foundation for the application of composite hydrogels in 3D bioprinting and biomedical applications.

3.1.3. Analysis of the Results of Chemical Structure Characterization of Hydrogels

The IR spectra of the composite hydrogels are shown in Figure 4A. The strong and broad band of 3000–3800 cm^{-1} is the absorption peak of the stretching vibration of the hydroxyl group (-OH). The peaks at 2930 cm^{-1}, 2850 cm^{-1}, and 1460 cm^{-1} are the main three absorption peaks of the methylene group of the protein contained in GEL. The IR characteristic peaks of GEL are also reflected in the peptide bonds, such as amide A and amide I–III [28–30]. The characteristic absorption peak of amide A (stretching vibration of N-H) is at 3273 cm^{-1}, the characteristic absorption peak of amide I (stretching vibration of C=O and C-N) is at 1650 cm^{-1}, the characteristic absorption peak of amide II (stretching vibration of N-H) is at 1550 cm^{-1}, and the characteristic absorption peak of amide III (stretching vibration of C-N) is at 1240 cm^{-1}. The stretching vibration peak of C-O is at 1050 cm^{-1}. The remaining absorption peaks at 923 cm^{-1}, 852 cm^{-1}, and 717 cm^{-1} are consistent with the standard IR spectra of GLY. As can be seen from Figure 4B, with the addition and increasing content of GLY, the characteristic peaks on the IR spectra of the hydrogels gradually agreed with those of glycerol, and the positions of the peaks did not shift significantly, which proved that no interaction occurred between GLY and both GEL and T-CNF.

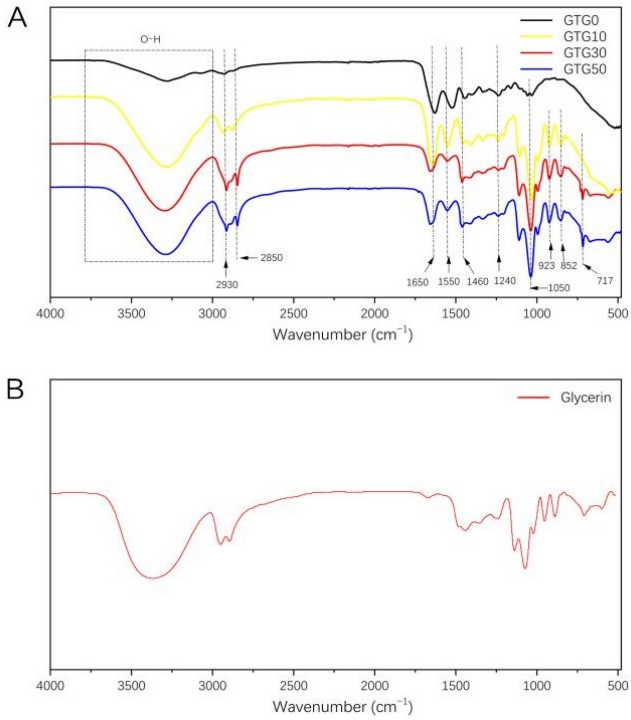

Figure 4. (**A**) Fourier-transform infrared spectra of GTG0, GTG10, GTG30, and GTG50, (**B**) Fourier-transform infrared spectra of Glycerin.

3.2. Analysis of Rheological Properties of Hydrogels

The shear-thinning properties of hydrogels are particularly important for extrusion-based 3D bioprinting methods. The shear-thinning property is a non-Newtonian fluid phenomenon in which the viscosity decreases rather than rises as the shear rate continues to increase. This is due to the temporary disruption of the physical interaction between macromolecules and macromolecules under high shear stress, resulting in the rearrangement of polymer chains and the reduction in segment entanglement. However, when the shear force disappears, the viscosity increases rapidly again, and this property is known as viscosity recovery. The shear-thinning property of the hydrogel allows the highly viscous hydrogel to pass through the nozzle smoothly, and the viscosity recovery property ensures that the hydrogel can have good shape fidelity after deposition on the platform. The "shear-thinning" and "viscosity recovery" phenomena experienced by hydrogels during 3D bioprinting are also known as "thixotropy".

Since hydrogels have special viscosity and elasticity, and the gel properties are sensitive to the load applied in the measurement process, the methods used in rheological testing are expected to have a certain impact on the structure and morphology of the gel, and it may be difficult to obtain the rheological data with good repeatability [31]. Therefore, suitable rheometer conditions should be selected to test the rheological properties of hydrogels, and the normal force load applied to hydrogels should be controlled. To eliminate the influence of the normal force on the rheological performance test, the normal force was recorded in real-time when the parallel plate reached the 2 mm gap until it reached the 2 mm gap [32]. In the process of realizing the set gap, the maximum load is up to 1.6 N, and a small load will not have a great impact on the structure of the hydrogel. Before formally starting the rheological test, allow the sample to relax the normal force and remove excess material.

The shear-thinning characteristics of the hydrogels were characterized at a temperature environment of 37 °C. As can be seen from Figure 5, when the shear rate was zero, and the shear rate was low, the viscosity of all four hydrogels was relatively high, and the initial viscosity also became higher with the increase in GLY content. When the shear rate gradually increases, the viscosity decreases rapidly. The shear rate variation curves show

that all four hydrogels have obvious shear-thinning characteristics and are suitable for extrusion 3D bioprinting.

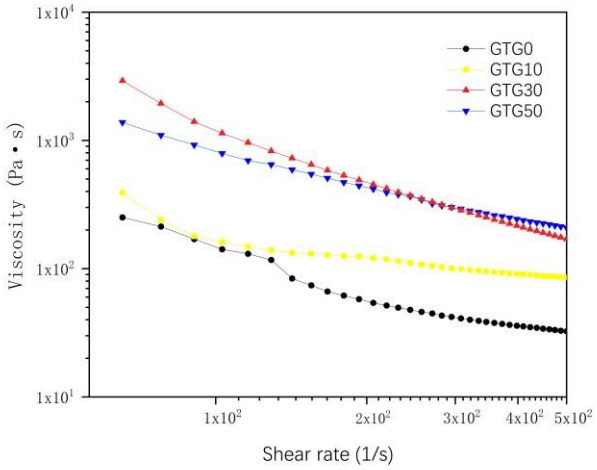

Figure 5. The viscosity-shear rate of hydrogels.

The storage modulus (G′) and loss modulus (G″) of the hydrogel are shown in Figure 6. The storage modulus (G′), also known as the elastic modulus, is the magnitude of energy stored in the material due to elastic (reversible) deformation when deformation occurs, reflecting the elasticity of the material. The loss modulus (G″), also known as the viscous modulus, is the magnitude of energy lost in the material due to viscous deformation (irreversible) when deformation occurs, reflecting the viscous size of the material. G′ and G″ are often used to characterize the mechanical properties of hydrogels, and the relationship between the two magnitudes can reflect the solid-liquid state of the material. When G' is greater than G″, the elastic deformation mainly occurs, and the hydrogel exhibits solid-like properties; when G′ is less than G″, the viscous deformation mainly occurs, and the hydrogel exhibits liquid-like properties.

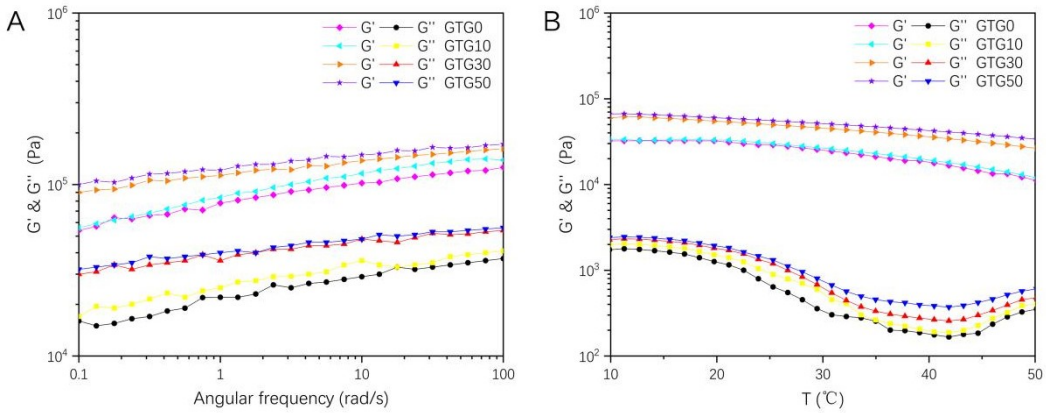

Figure 6. The rheological properties change curves of the hydrogel: (**A**) The storage modulus (G′) and loss modulus (G″)-angular frequency of GTG0, GTG10, GTG30, and GTG50, (**B**) The storage modulus (G′) and loss modulus (G″)-temperature of GTG0, GTG10, GTG30, and GTG50.

The oscillation-angular frequency curves of hydrogels are shown in Figure 6A, and it can be found that both G′ and G″ of the four groups of hydrogels increase with the increase in the angular frequency, and the curve of G′ is always higher than G″, with no crossover point. This indicates that the hydrogels exhibit a solid-like gel elastic network structure, which is conducive to improving the shape stability and structural fidelity of the printed structures. Compared with the hydrogel without GLY addition, the G′ and G″ of GTG10,

GTG30, and GTG50 gradually increase, which is because the addition of GLY reduces the water content in the hydrogel.

The oscillation-temperature curves of the hydrogel are shown in Figure 6B, and it can be found that both G′ and G″ of the hydrogel decrease as the temperature increases, but G′ is still always much larger than G″, which indicates that the hydrogel network remains stable when the temperature changes and the system always has a solid-like hydrogel property.

3.3. Analysis of Mechanical Properties of Hydrogels

The improvement and modulation of the mechanical properties of hydrogels are crucial for the application of 3D bioprinting. Proper mechanical stability is required during 3D printing; the printed structures must also have strong physical properties and be resistant to compression to provide support for cells and tissues.

Figure 7 shows the experimental results of the compressive strength of the hydrogels. It can be seen that there are significant differences in the mechanical properties of the four hydrogels, but all of them have a certain compressive strength and good compressive properties, which are compressive materials. The maximum compressive strength of the composite hydrogel GTG0 without the addition of GLY is 198 KPa, the maximum compressive strength of the composite hydrogel is significantly increased after the addition of GLY, and the maximum compressive strength of GTG10 is 350 KPa, and the maximum compressive strength of GTG30 is 403 KPa. The maximum compressive strength of GTG50 was 392 KPa, which was slightly lower than that of GTG30 because the increasing GLY content also made the internal pore structure of the hydrogel too dense, thus negatively affecting the compressive strength. The experimental results showed that the compressive performance of the hydrogel compounded with GLY was significantly better than that of the gelatin-oxidized nanocellulose hydrogel, and the compressive performance of the hydrogel improved with increasing GLY content at less than 50% w/v.

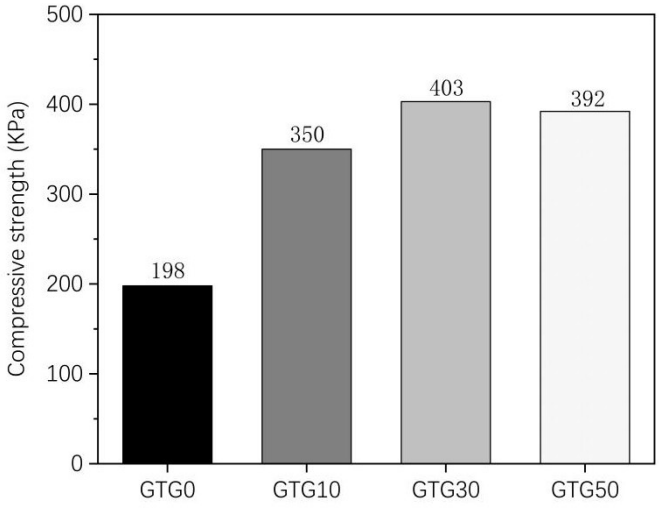

Figure 7. Compressive strength of GTG0, GTG10, GTG30, and GTG50.

3.4. Analysis of Swelling Properties of Hydrogels

Proper water swelling and porosity are favorable for the transport and exchange of nutrients in the printed structure, and the aqueous condition is favorable for the growth of cells. Thus, the swelling ratio is a very important indicator of hydrogel. Figure 8A shows the swelling ratio of the hydrogel samples obtained from the experiment. It can be seen that the sample swells rapidly in the first 3 h, and the swelling decreases significantly after 12 h until the swelling equilibrium is reached at 24 h. After 24 h, the swelling of the sample only fluctuates slightly. As shown in Figure 8B, the swelling ratio of GTG0 was 837%, and that of GTG50 was 691%, which were significantly different from each other. It can be found that the swelling ratio of hydrogel decreases with the increase in GLY content,

and the swelling performance is negatively affected. On the one hand, it is due to the enhanced intermolecular hydrogen bonding and mutual entanglement after the addition of T-CNF, which makes the intermolecular interaction tighter and the hydrogel structure relatively dense. On the other hand, it is because the addition of GLY further reduces the water content and increases the solid content. Thus, the water absorption and swelling ratio decreases.

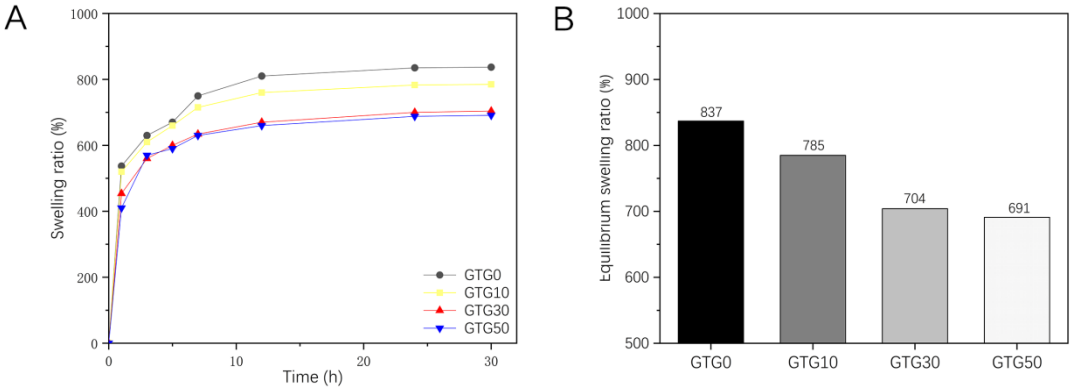

Figure 8. The swelling properties of GTG0, GTG10, GTG30, and GTG50: (**A**) Variation curve of swelling ratio with time, (**B**) Equilibrium swelling ratio.

3.5. Analysis of Printing Properties of Hydrogels

Good printing performance is always a challenge throughout the development process of materials suitable for biological 3D printing. From the perspective of tissue engineering research, materials applied to bioprinting need to provide a certain mechanical strength while satisfying biocompatibility for subsequent histochemical culture and implantation experiments. GEL, as the most common hydrogel matrix component, provides a well-defined function in bioink. As a degradation product of collagen, GEL is naturally biocompatible and is one of the main components of the extracellular matrix, providing the microenvironment necessary for cellular components to adhere and proliferate. On the other hand, GEL has temperature-sensitive phase transition properties that are lacking in colloidal materials, with a gel state at low temperatures and increased fluidity with increasing temperature. Therefore, the main function of the GEL component in the hydrogel is to provide a cell survival environment as well as a temperature-sensitive glue-forming capability. However, the glue-forming capability of the GEL is reversible. In the cell incubation environment (37 °C), GEL dissolves rapidly, and other materials need to be added to enhance the mechanical strength to ensure the stability of the bioprinted structure. However, from a bioprinter's perspective, the material cannot be mechanically enhanced without limits. Its mechanical properties are governed by the extrusion-based printing technology, both in terms of maintaining sufficient fluidity during extrusion to minimize shear damage to the cellular components by the extrusion head and to reduce nozzle clogging and in terms of providing mechanical support during the setting process and after cross-linking. Therefore, the addition of T-NFC can provide the hydrogel with suitable mechanical properties for the size so that it can enhance the printability and fidelity of the hydrogel while achieving self-support of the hydrogel structure during the printing process, which has great potential for application. When the GTG0 hydrogel without GLY was directly used for extrusion-based 3D bioprinting, it was found that the hydrogel would naturally flow out when no printing pressure was applied, and the extrusion was not stable and smooth enough under the low printing pressure, which affected the printing accuracy and printing molding situation. Because the bio-ink is greatly affected by the printing pressure, the thickness of the silk thread is easily unstable. Where the thread is wider, there will be a certain degree of accumulation and diffusion, and where the thread is narrow, the thread may even be broken, and the nozzle will be blocked. This is due to the material's low

viscosity, relatively small solid content, and low mechanical strength, and the material cannot provide sufficient support for the superstructure on the deposition platform.

To avoid structure collapse after printing and to increase the viscosity of the hydrogel, we replaced part of the water with GLY and reduced the volume and share of the non-volatile components. GTG10, GTG30, and GTG50 were used directly for extrusion printing. In addition, the grid structure and hollow circular tube structure were designed to evaluate the shape fidelity. The area fidelity parameters of the grid structure are calculated by Equation (2).

$$F_g(\%) = \frac{S_a}{S_t} \times 100\% \quad (2)$$

where S_a is the actual grid area and S_t is the theoretical grid area. The area fidelity of the three hydrogels is shown in Figure 9.

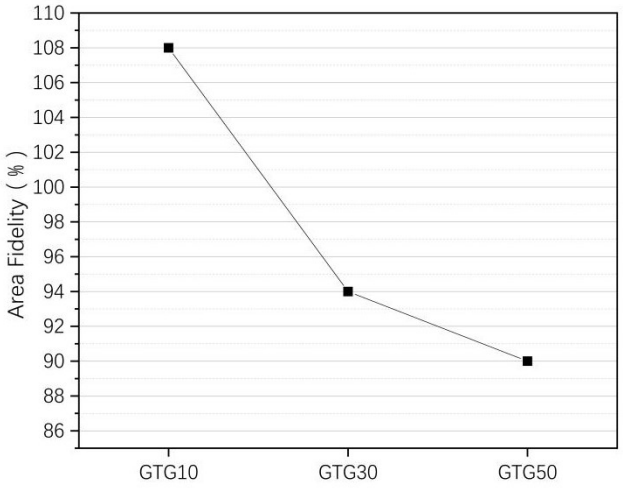

Figure 9. The area fidelity of GTG10, GTG30, and GTG50.

When the GLY addition content is small, the viscosity of the hydrogel is not significantly increased, resulting in a certain degree of accumulation and diffusion, which makes the area fidelity of the grid structure are poor, and the printed grid structure area significantly larger than the theoretical grid area. When the GLY content continues to increase, with the increase in the viscosity and solid content of the hydrogel, the printed structure area is closer to the theoretical area.

The F_g of GTG30 is about 94%. The printed grid structure has a clear outline and uniform grid with the highest fidelity. The F_g of GTG50 decreases by about 90% because the hydrogel viscosity is too large and the silk thread is too thin at the same printing air pressure, which affects the grid structure outline and molding effect. After increasing the printing air pressure appropriately, the situation of too-thin silk thread will be improved significantly and F_g will be improved.

The height fidelity parameter of the hollow circular tube structure is calculated by Equation (3).

$$F_h(\%) = \frac{h_a}{h_t} \times 100\% \quad (3)$$

where h_a is the actual height and h_t is the theoretical height. The theoretical maximum number of printed layers is set to 100 layers, and the height of each layer is 0.2 mm. The high fidelity and the maximum number of printed layers of the hollow circular tube structure of the three hydrogel materials are shown in Figure 10.

The use of printing a hollow circular tube structure can measure the degree of spreading and sinking of the thread. As can be seen in Figure 10B, the maximum number of printed layers for GTG10 is only 26, while both GTG30 and GTG50 can reach the set maximum number of 100 layers. This is due to the fact that at lower GLY content, there is still a

more serious diffusion of the thread, and when the number of printed layers exceeds 20, there is an obvious tendency of sinking and collapse, resulting in a lower number of printed layers and poorer high fidelity. With the increase in GLY content, the maximum number of printed layers of hydrogel appears to increase significantly and still has a good molding effect when printing 100 layers. The high fidelity of the GTG10, GTG30, and GTG50 is shown in Figure 10A, among which the highest high fidelity of GTG30 is about 90%, which proves that the thread-forming effect on the top layer of the circular tube structure is better and the structural stability is high. However, when the number of printed layers is too high, the hydrogel is too far from the low-temperature deposition platform, resulting in uneven temperature transfer and too high temperature of the upper layer, and the middle and upper part of the printed structure shows deformation and slight deposition, which forms a certain impact on the high fidelity.

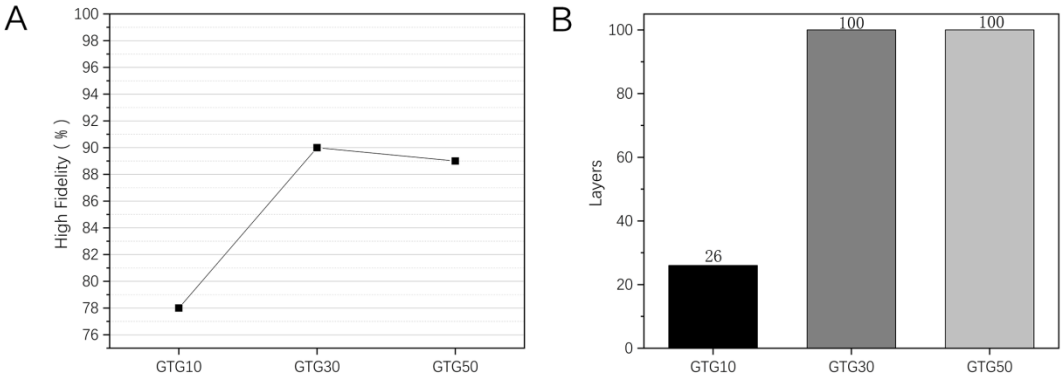

Figure 10. Printing of hollow circular tube structure with GTG10, GTG30, GTG50: (**A**) High fidelity, (**B**) the Maximum number of printed layers.

Through the study of the area fidelity of the grid structure and the circular tube structure, it can be seen that the area fidelity and height fidelity of GTG10 are not as good as GTG30 and GTG50, of which GTG30 has the best performance. As can be seen in Figure 11, it can be found that GTG30 has good printability, the printing thread is continuous and clear, there is no obvious broken thread and collapse during the printing process, and the complex three-dimensional structure also has high printing accuracy.

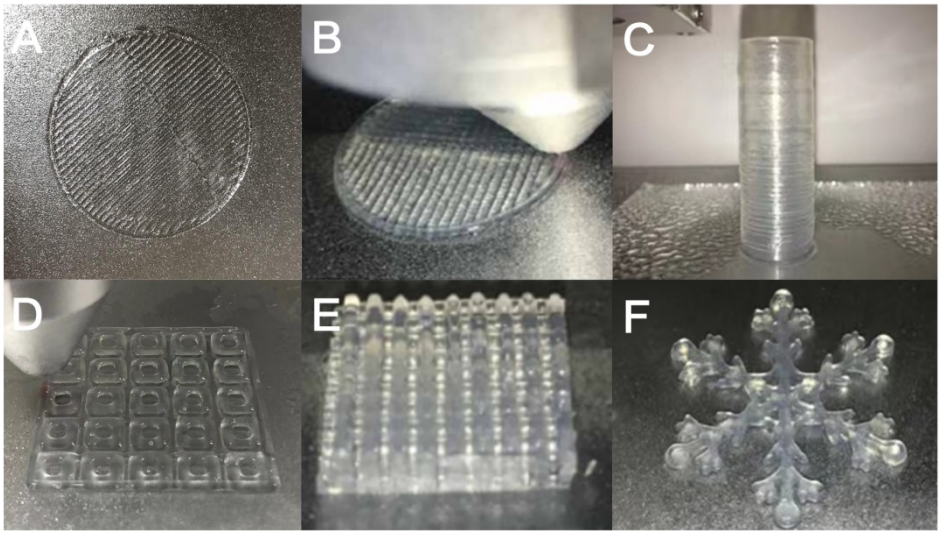

Figure 11. GTG30 for complex structure printing: (**A**) single-layer grid structure, (**B**) double-layer grid structure, (**C**) hollow circular tube structure, (**D**) single-layer grid support, (**E**) multi-layer grid support, (**F**) snowflake special structure.

4. Conclusions

In this study, by introducing GLY as a multifunctional co-solvent into the gelatin-oxidized nanocellulose-based hydrogels, we successfully prepared composite hydrogels with good pore structure and mechanical properties that can be suitable for extrusion-based 3D bioprinting and determined the most suitable hydrogel ratios by material characterization methods and 3D printing experiments. Macroscopic morphological analysis showed that the addition of GLY had a stabilizing effect on the hydrogels and did not affect the gel properties. Scanning electron microscopy results also showed that the composite hydrogels had high porosity, in which GTG30 had a uniform distribution of microporous structure and uniform pore size. By increasing the share of non-volatile components and using effective strength additives such as T-CNF, good shear-thinning properties are imparted to the composite hydrogels so that the system always has solid-like hydrogel properties, avoiding collapse during printing, and increasing the shape fidelity and stability of the printed structures. We also tested the compressive strength of the four composite hydrogels, and the results showed that GTG30 has better swelling, the highest compressive strength, and the best mechanical properties. Several tests have shown that the composite hydrogel GTG30 has the best overall performance in all aspects and is the best ratio that can be applied to extrusion-based 3D bioprinting. A series of printing experiments followed, demonstrating that GTG30 has better printability, structural stability, and shape fidelity than other hydrogel ratios. The results of various tests indicate that the composite hydrogel with gelatin-oxidized nanocellulose as the matrix and glycerol as the multifunctional co-solvent can provide new material and ideas for 3D bioprinting and expand the potential use of the material.

Author Contributions: Conceptualization, S.Z. and Z.N.; methodology, S.Z.; validation, S.Z., C.H. and Z.N.; data curation, C.Y.; writing—original draft preparation, S.Z.; writing—review and editing, Z.N. and C.H.; supervision, Y.N. and Y.L.; project administration, S.Z., C.H. and Z.N. All authors have read and agreed to the published version of the manuscript.

Funding: This work was found by the Planning Project of Application Research for Public Service Technology of Zhejiang Province (LGG18E060002), the Zhejiang Provincial Collaborative Innovation Center for Bamboo Resources and High-efficiency Utilization (2017ZZY2-15), and the Opening Project of Zhejiang Province Key Laboratory for Digital Design and Intelligent Manufacturing of Cultural Characteristics and Creative Products (ZD201803).

Institutional Review Board Statement: Not applicable.

Informed Consent Statement: Not applicable.

Data Availability Statement: Not applicable.

Conflicts of Interest: The authors declare no conflict of interest.

References

1. Wu, J.; Guo, J.; Linghu, C.; Lu, Y.; Song, J.; Xie, T.; Zhao, Q. Rapid digital light 3D printing enabled by a soft and deformable hydrogel separation interface. *Nat. Commun.* **2021**, *12*, 6070. [CrossRef] [PubMed]
2. Zhang, Y.Y.; Jin, Z.J.; Zhang, W. Application of 3D Printing in Future Manned Space Exploration. *Mater. Sci. Forum.* **2020**, *982*, 92–97. [CrossRef]
3. Ballard, D.H.; Mills, P.; Duszak, R.; Weisman, J.A.; Rybicki, F.J.; Woodard, P.K. Medical 3D Printing Cost-Savings in Orthopedic and Maxillofacial Surgery: Cost Analysis of Operating Room Time Saved with 3D Printed Anatomic Models and Surgical Guides. *Acad. Radiol.* **2020**, *27*, 1103–1113. [CrossRef] [PubMed]
4. Rency, G.; Lakshmi, T.S.; Anugya, B.; Naresh, K.; Renjith, P.N. Development and evaluation of a multicomponent bioink consisting of alginate, gelatin, diethylaminoethyl cellulose and collagen peptide for 3D bioprinting of tissue construct for drug screening application. *Int. J. Biol. Macromol.* **2022**, *207*, 278–288. [CrossRef]
5. Felix, K.; Sophie, D.; Johannes, W.; Julia, E.; Franziska, H.; Maria, M.M.; Juliane, S.; Thomas, W.; Michael, K.; Michael, G.; et al. Think outside the box: 3D bioprinting concepts for biotechnological applications-recent developments and future perspectives. *Biotechnol. Adv.* **2022**, *58*, 107930. [CrossRef]
6. Luo, Y.; Lin, X.; Huang, P. 3D Bioprinting of Artificial Tissues: Construction of Biomimetic Microstructures. *Macromol. Biosci.* **2018**, *18*, e1800034. [CrossRef]

7. Fatimi, A.; Okoro, O.V.; Podstawczyk, D.; Siminska-Stanny, J.; Shavandi, A. Natural Hydrogel-Based Bio-Inks for 3D Bioprinting in Tissue Engineering: A Review. *Gels* **2022**, *8*, 179. [CrossRef]
8. Song, D.; Xu, Y.; Liu, S.; Wen, L.; Wang, X. Progress of 3D Bioprinting in Organ Manufacturing. *Polymers.* **2021**, *13*, 3178. [CrossRef]
9. Dai, L.; Cheng, T.; Duan, C.; Zhao, W.; Zhang, W.P.; Zou, X.J.; Aspler, J.; Ni, Y.H. 3D Printing Using Plant-derived Cellulose and Its Derivatives: A Review. *Carbohydr. Polym.* **2018**, *203*, 71–86. [CrossRef]
10. Gary, C.C. Potential and Limitations of Nanocelluloses as Components in Biocomposite Inks for Three-Dimensional Bioprinting and for Biomedical Devices. *Biomacromolecules* **2018**, *19*, 701–711. [CrossRef]
11. Müller, M.; Öztürk, E.; Arlov, Ø.; Paul, G.; Marcy, Z.W. Alginate Sulfate–Nanocellulose Bioinks for Cartilage Bioprinting Applications. *Ann. Biomed. Eng.* **2017**, *45*, 210–223. [CrossRef] [PubMed]
12. Mandrycky, C.; Wang, Z.; Kim, K.; Kim, D.H. 3D bioprinting for engineering complex tissues. *Biotechnol. Adv.* **2016**, *34*, 422–434. [CrossRef] [PubMed]
13. Kumar, P.; Ebbens, S.; Zhao, X.B. Inkjet printing of mammalian cells-Theory and applications. *Bioprinting* **2021**, *23*, e00157. [CrossRef]
14. Zheng, Z.Z.; Eglin, D.; Alini, M.; Richards, G.R.; Qin, L.; Lai, Y.X. Visible light-induced 3D bioprinting technologies and corresponding bioink materials for tissue engineering: A review. *Engineering* **2020**, *7*, 966–978. [CrossRef]
15. Chameettachal, S.; Yeleswarapu, S.; Sasikumar, S.; Shukla, P.; Hibare, P.; Bera, A.K.; Bojedla, S.S.; Pati, F. 3D Bioprinting: Recent Trends and Challenges. *J. Indian Inst. Sci.* **2019**, *99*, 375–403. [CrossRef]
16. Fu, Z.; Naghieh, S.; Xu, C.; Wang, C.; Sun, W.; Chen, X. Printability in extrusion bioprinting. *Biofabrication* **2021**, *3*, 13. [CrossRef]
17. Sungchul, S.; Soohyun, P.; Minsung, P.; Eunsue, J.; Kyunga, N.; Hye, J.Y.; Jinho, H. Cellulose Nanofibers for the Enhancement of Printability of Low Viscosity Gelatin Derivatives. *BioResources* **2017**, *12*, 2941–2954. [CrossRef]
18. Ragab, E.A.; Ramzi, K.; Davide, B.; Alain, D. Biomimetic Mineralization of Three-Dimensional Printed Alginate/TEMPO-Oxidized Cellulose Nanofibril Scaffolds for Bone Tissue Engineering. *Biomacromolecules* **2018**, *19*, 4442–4452. [CrossRef]
19. Kirchmajer, D.M.; Gorkin, I.R.; Panhuis, M.I.H. An overview of the suitability of hydrogel-forming polymers for extrusion-based 3D-printing. *J. Mat. Chem. B* **2015**, *3*, 4105–4117. [CrossRef]
20. Alruwaili, M.; Lopez, J.A.; McCarthy, K.; Reynaud, E.G.; Rodriguez, B.J. Liquid-phase 3D bioprinting of gelatin alginate hydrogels: Influence of printing parameters on hydrogel line width and layer height. *Bio-Des. Manuf.* **2019**, *2*, 172–180. [CrossRef]
21. Fan, C.J.; Wang, D.A. Macroporous Hydrogel Scaffolds for Three-Dimensional Cell Culture and Tissue Engineering. *Tissue Eng. Part B-Rev.* **2016**, *23*, 451–461. [CrossRef] [PubMed]
22. Jisun, P.; Jin, S.L.; Solchan, C.; Jun, H.L.; Wan, K.D.; Jae, Y.L.; Su, A.P. Cell-laden 3D bioprinting hydrogel matrix depending on different compositions for soft tissue engineering: Characterization and evaluation. *Mater. Sci. Eng. C.* **2017**, *71*, 678–684. [CrossRef]
23. Wang, S.; Lee, J.M.; Yeong, W.Y. Smart hydrogels for 3D bioprinting. *Int. J. Bioprint.* **2015**, *1*, 3–14. [CrossRef]
24. Nguyen, D.; Hägg, D.A.; Forsman, A.; Ekholm, J.; Nimkingratana, P.; Brantsing, C.; Kalogeropoulos, T.; Zaunz, S.; Concaro, S.; Brittberg, M.; et al. Cartilage Tissue Engineering by the 3D Bioprinting of iPS Cells in a Nanocellulose/Alginate Bioink. *Sci. Rep.* **2017**, *7*, 658. [CrossRef] [PubMed]
25. Ahmad, R.; Kamal, M.; Ellinor, B.H.; Kristin, S. Cytocompatibility of Wood-Derived Cellulose Nanofibril Hydrogels with Different Surface Chemistry. *Biomacromolecules* **2017**, *18*, 1238–1248. [CrossRef]
26. Baumgartner, M.; Hartmann, F.; Drack, M. Resilient yet entirely degradable gelatin-based biogels for soft robots and electronics. *Nat. Mater.* **2020**, *19*, 1102–1109. [CrossRef]
27. Dai, H.J.; Li, X.Y.; Du, J.; Ma, L.; Yu, Y.; Zhou, H.Y.; Guo, T.; Zhang, Y.H. Effect of interaction between sorbitol and gelatin on gelatin properties and its mechanism under different citric acid concentrations. *Food Hydrocoll.* **2020**, *101*, 105557. [CrossRef]
28. Sultan, S.; Mathew, A.P. 3D printed scaffolds with gradient porosity based on a cellulose nanocrystal hydrogel. *Nanoscale* **2018**, *10*, 4421–4431. [CrossRef]
29. Naseri, N.; Deepa, B.; Mathew, A.P.; Oksman, K.; Girandon, L. Nanocellulose-Based Interpenetrating Polymer Network (IPN) Hydrogels for Cartilage Applications. *Biomacromolecules* **2016**, *17*, 3714–3723. [CrossRef]
30. Avik, K.; Ruhul, A.K.; Stephane, S.; Canh, L.T.; Bernard, R.; Jean, B.; Gregory, C.; Victory, T.; Musa, R.K.; Monique, L. Mechanical and barrier properties of nanocrystalline cellulose reinforced chitosan based nanocomposite films. *Carbohydr. Polym.* **2012**, *90*, 1601–1608. [CrossRef]
31. Jürgen, K.; Svetlana, R.D. Interfacial shear rheology. *Curr. Opin. Colloid Interface Sci.* **2010**, *15*, 246–255. [CrossRef]
32. Liparoti, S.; Speranza, V.; Marra, F. Alginate hydrogel: The influence of the hardening on the rheological behaviour. *J. Mech. Behav. Biomed. Mater.* **2021**, *116*, 104341. [CrossRef] [PubMed]